A physical explanation of the variation in threshold for delineating terrestrial water surfaces from multi-temporal images: effects of radiometric correction

Yuanbo Liu [a] , Ping Song [a] , Jian Peng [a] & Chun Ye [a]

[a] State Key Laboratory of Lake Science and Environment , Nanjing Institute of Geography and Limnology, Chinese Academy of Sciences , Nanjing , 200008 , PR China
Published online: 05 Apr 2012.

PLEASE SCROLL DOWN FOR ARTICLE

A physical explanation of the variation in threshold for delineating terrestrial water surfaces from multi-temporal images: effects of radiometric correction

YUANBO LIU*, PING SONG, JIAN PENG and CHUN YE

State Key Laboratory of Lake Science and Environment, Nanjing Institute of Geography and Limnology, Chinese Academy of Sciences, Nanjing 200008, PR China

Multi-temporal satellite images are widely used to delineate objects of interest for monitoring surface changes. Threshold value(s) are often determined from a histogram of a delineation index. However, the threshold determined may vary and be case-dependent, with images taken at different times. Although the variation is well known, its cause remains unclear, and this raises doubts about the reliability of the classification results. This study selects three widely used indices, the near-infrared (NIR) band, the normalized difference vegetation index (NDVI) and the normalized difference water index (NDWI), all of which can be used to delineate water surfaces. Our theoretical analysis reveals that sensor calibration, the Sun–target–satellite geometry and the atmospheric optical properties create synthetic effects on the satellite's digital number (DN) and, subsequently, on the thresholds for delineation. The DN-based threshold has a significant dependence on the reflectance-based counterpart, which has been proved with multi-temporal Moderate Resolution Imaging Spectroradiometer (MODIS) data for the Poyang Lake region of China. Our results show that a DN-based threshold is generally higher than a reflectance-based one, and ~90% of the difference is accounted for by temporal influences. A quantification of the temporal influences provides a physical explanation to the variation in thresholds, and the findings should be valuable for improving the reliability of long-term studies using multi-temporal images.

1. Introduction

Numerous satellite sensors have been launched into orbit for the long-term monitoring of our changing Earth (Committee on Earth Observation Satellites 2010). Surface objects of interest and changes in them can be extracted with a classification approach from multi-temporal satellite data (Pala and Pal 1993, Cheng *et al.* 2001). The primary principle of the application of environmental remote sensing to the classification of surface objects is that each object has a unique electromagnetic spectrum that makes it unique (Cracknell and Hayes 2007). The simplest approach to classification is to utilize a single band or to transform multiple bands of satellite image(s) into a new index in order to generate a histogram. From the histogram, the objects are often separated from their background with optimal threshold value(s) (Otsu 1979).

*Corresponding author. Email: ybliu@niglas.ac.cn; yb218@yahoo.com

In addition to the inherent optical properties of surface objects, remotely sensed data vary with time due to factors such as varying Sun–target–satellite geometry, atmospheric conditions and sensor degradation (Schott *et al*. 1988, Yuan and Elvidge 1996, Liu *et al*. 2006). Given the multi-temporal images, the threshold value(s) determined may vary and be case-dependent in delineating the same object at different times. This variation is widely known to exist, yet it remains unclear as to how the threshold value varies and upon what factors it depends. The use of variant threshold values without any physical basis raises doubts about the reliability of classification results. In a study of aerosol optical thickness (AOT), Tanre *et al*. (1988) found that in histograms, the variation of apparent reflectance of nearly unchanging ground is related to the variation in atmospheric optical properties. However, they did not go further to address the threshold variation. In our recent study on an algal bloom area extracted from multi-temporal images using both a single-band approach and a band ratio delineation approach, we reported that the optimal threshold values from histograms had a statistically significant dependence on AOT and the solar zenith angle (SZA) (Zhang *et al*. 2009). Yet, the study did not explain the physical basis of the dependence.

In this study, we attempt to offer for the first time a theoretical basis for the variation of threshold value(s) in multi-temporal image delineation. We choose three indices that are widely used for delineation in remote-sensing applications. The indices include the single near-infrared (NIR) band, the normalized difference vegetation index (NDVI) and the normalized difference water index (NDWI). Among all land objects, water is the surface that is most easily discerned by optical remote sensing. Because we do not intend to study the effectiveness of any delineation approach but want to explore the threshold variation in delineation from multi-temporal images, we select water surface as our object. All the three indices can be used to extract inland water surface (Richard and Mary 1988, Goward *et al*. 1991, McFeeters 1996). We use theoretical analysis to quantify the temporal factors imposed on satellite images and the subsequent thresholds. For a case study, we use Moderate Resolution Imaging Spectroradiometer (MODIS) Level-1B data to inspect and evaluate the temporal influences on thresholds. Finally, we discuss the potential use of our findings for remote-sensing applications.

2. Methodology

Bi-level thresholding of an object from its background in an image may be expressed as

$$f(x) = \begin{cases} \text{object} & (x \leq t) \\ \text{background} & (x > t) \end{cases}, \tag{1}$$

where $f(x)$ denotes an extract function, a pixel in an image is defined as an 'object' or 'background', x is a value in a band of the image or a value transformed from multiple bands and t is the threshold. A thresholding algorithm or technique may be used to determine a threshold value. As a result of the thresholding, the image is separated into the object and the background.

In remote sensing, either a single band or a transformed index can be used to delineate water surfaces (Richard and Mary 1988, Goward *et al*. 1991, McFeeters 1996). The NIR band is often selected for the delineation because it is not only strongly absorbed by water but also strongly reflected by terrestrial vegetation and

soil (McFeeters 1996). Water reflects most visible wavelengths, and the visible band is often combined with the NIR band to generate a transformed index. Examples include NDVI and NDWI, which are defined as

$$\text{NDVI} = \frac{\rho_{\text{NIR}} - \rho_{\text{R}}}{\rho_{\text{NIR}} + \rho_{\text{R}}} \tag{2a}$$

and

$$\text{NDWI} = \frac{\rho_{\text{G}} - \rho_{\text{NIR}}}{\rho_{\text{G}} + \rho_{\text{NIR}}}, \tag{2b}$$

where ρ_{NIR} is the surface reflectance in the NIR band, ρ_{R} is the reflectance value in the red band and ρ_{G} is the reflectance value in the green band. The sharp contrast between the surface of water and other objects enables the threshold values to be easily determined from a histogram of a NIR, NDVI or NDWI index.

In practice, both the surface reflectance and satellite digital number (DN) have been used to calculate NDVI or NDWI (e.g., Carlson and Ripley 1997, Teillet *et al.* 1997). Because void values are common in surface reflectance products, satellite DN data are often preferable for water surface delineation. In this case, NDVI and NDWI are expressed as

$$\text{NDVI}_{\text{DN}} = \frac{(\text{DN})_{\text{NIR}} - (\text{DN})_{\text{R}}}{(\text{DN})_{\text{NIR}} + (\text{DN})_{\text{R}}} \tag{3a}$$

and

$$\text{NDWI}_{\text{DN}} = \frac{(\text{DN})_{\text{G}} - (\text{DN})_{\text{NIR}}}{(\text{DN})_{\text{G}} + (\text{DN})_{\text{NIR}}}, \tag{3b}$$

where $(\text{DN})_{\text{NIR}}$, $(\text{DN})_{\text{R}}$ and $(\text{DN})_{\text{G}}$ are the DN in the NIR, red and green bands, respectively. Atmosphere- and/or sensor-induced variation in the DN may result in a variation of NDVI (Carlson and Ripley 1997, Xiao *et al.* 2003, van Leeuwen *et al.* 2006) and NDWI and a variation in the subsequent determination of threshold values.

Variation in DN comes from changes in the spectral properties of a surface as well as from several other sources. The major time-dependent factors involve the Sun–target–satellite geometry, atmospheric optical properties and sensor calibration (Schott *et al.* 1988, Yuan and Elvidge 1996, Liu *et al.* 2006). These factors impose temporal influences on the DN but are independent of surface reflectance. For a Lambertian surface, an analytical form of the DN value of a pixel can be expressed with the imposed influences for a reflective band (Liu *et al.* 2011):

$$\text{DN} = \frac{T_{\text{g}} T_{\text{s}} T_{\text{v}} G \cos\theta}{G_0 d^2} [\text{DN}]_0 - \frac{T_{\text{g}} T_{\text{s}} T_{\text{v}} G \cos\theta}{G_0 d^2} B_0 + B + \rho_{\text{a}} \frac{T_{\text{g}} E G \cos\theta}{\pi d^2}, \tag{4}$$

where G is the band-specific sensor calibration gain (in DNs per unit radiance), B is the band-specific sensor calibration bias (in DNs) for zero radiance, d is the Sun–Earth distance in astronomical units, E is the band-specific exo-atmospheric solar irradiance (W m^{-2} μm^{-1}), θ is the SZA, ρ_{a} is the intrinsic atmospheric reflectance due to

Rayleigh and aerosol scattering, T_g is atmospheric absorption, T_s is the total downward atmospheric transmission along the Sun–target path and T_v is the total upward atmospheric transmission along the target–satellite path. The subscript 0 in variables such as $[DN]_0$ denotes the pixel value taken at an ideal or standardized condition. For example, $d_0 = 1$, and $[DN]_0$ is taken at the nadir-view when the Sun is at its zenith under an atmosphere-free condition and without sensor degradation. In this case, we may derive the following expression for $[DN]_0$ (see Appendix A):

$$[DN]_0 = G\frac{\rho E}{\pi} + B, \tag{5}$$

where ρ is the surface reflectance in a specific reflective band (Liu *et al.* 2006, 2011). In this case, the reflectance can be ρ_{NIR}, ρ_R or ρ_G.

Equations (4) and (5) mathematically link at-satellite DN to at-surface reflectance. Provided the atmosphere is basically homogeneous under a clear sky, temporal influences may alter the statistical properties of an image, but the relative relationship among pixel features will be retained. The imposed influences may affect the absolute position of a pixel in a histogram but not the relative distribution of the pixel among the image pixels. If there are no changes in the surface spectrum, the variation in threshold value(s) should be primarily attributed to temporal influences.

MODIS has a complete set of on-board calibrators (Xiong *et al.* 2009), and its sensor calibration gain is updated routinely such that the sensor calibration bias is zero ($B = 0$). For MODIS Level-1B, the raw digital signals measured at reflective band detectors are corrected for all the known instrument effects to produce the corrected DN (NASA 2006). A Level-1B product contains both calibrated and geolocated at-aperture radiances. In this case, $T_v = 1$. The DN value in a reflective band is then simplified to

$$DN = \frac{T_g T_s \cos\theta}{d^2}[DN]_0 + \rho_a \frac{T_g E G \cos\theta}{\pi d^2}. \tag{6}$$

From equations (5) and (6), we have a DN value in the NIR band of

$$DN_{NIR} = \frac{T_{g,NIR} E_{NIR} G_{NIR} \cos\theta}{\pi d^2}\left(T_{s,NIR}\rho_{NIR} + \rho_{a,NIR}\right). \tag{7a}$$

From equations (2)–(6), we obtain the following relationship between NDVI and NDVI thresholds for DN ($NDVI_{DN}$):

$$\frac{1 - [NDVI]_{DN}}{1 + [NDVI]_{DN}} = \frac{T_{g,R} E_R G_R}{T_{g,NIR} E_{NIR} G_{NIR}}\left(\frac{T_{s,R}\rho_{NIR}}{T_{s,NIR}\rho_{NIR} + \rho_{a,NIR}}\frac{1 - [NDVI]}{1 + [NDVI]} + \frac{\rho_{a,R}}{T_{s,NIR}\rho_{NIR} + \rho_{a,NIR}}\right). \tag{7b}$$

Likewise, the relationship between NDWI and $NDWI_{DN}$ is given in the following equation:

$$\frac{1 - [NDWI]_{DN}}{1 + [NDWI]_{DN}} = \frac{T_{g,NIR} E_{NIR} G_{NIR}}{T_{g,G} E_G G_G}\left(\frac{T_{s,NIR}\rho_G}{T_{s,G}\rho_G + \rho_{a,G}}\frac{1 - [NDWI]}{1 + [NDWI]} + \frac{\rho_{a,NIR}}{T_{s,G}\rho_G + \rho_{a,G}}\right). \tag{7c}$$

Because MODIS spectral reflective bands are well placed to avoid most atmospheric absorption features (Barnes *et al*. 1998, van Leeuwen *et al*. 2006, Chander *et al*. 2010), T_g is approximately equal to unity and can be ignored in equations (7a)–(7c).

In general, equations (7a)–(7c) reveal that satellite DN-based values are a function of band-specific sensor gain, atmospheric transmission, path radiance and surface reflectance. In other words, the senor gain, atmospheric transmission and path radiance imposed on the surface reflectance offer explanations for the variations in DN-based values and subsequent thresholds.

3. Data and processing

MODIS products over the Poyang Lake region of China, located at 28° 22′–29° 45′ N, 115° 47′–116° 45′ E in a humid subtropical climate zone, were obtained. The dominant land covers include water, wetland vegetation, agricultural fields, grassland and bare land surfaces. The Poyang Lake wetland is well known as a part of the Ramsar Convention List of Wetlands of International Importance. It has important hydrological, biological, ecological and economic consequences.

MODIS images of the study area were selected for 33 cloud-free dates in 2008. MOD02_QKM, MOD02_HKM, MOD03_L1A, MOD04_L2 and MOD09 data were obtained from the Warehouse Inventory Search Tool (https://wist.echo.nasa.gov/). The data were generated from the Product Generation Executive (PGE) code, Version 5 (http://modis-sdst.gsfc.nasa.gov/). The MOD02_QKM and MOD02_HKM data sets contain both Level-1B calibrated and geolocated at-aperture radiances for visible and NIR bands (Masuoka *et al*. 1998). The MOD02_HKM data sets were used to extract DN values in the green band (0.545–0.565 µm) at 500 m resolution, and the MOD02_QKM data sets were used to extract DN values in the red band (0.62–0.67 µm) and the NIR band (0.841–0.876 µm) at 250 m resolution. The MOD03_L1A geolocation product contains geodetic coordinates, solar zenith and azimuth angles for each MODIS pixel (Wolfe *et al*. 2002). The data sets were used to calculate the Sun–target–satellite geometry parameters. The MOD04_L2 data contain the ambient AOT (0.47, 0.55 and 0.66 µm) and path radiance (0.47 and 0.66 µm) at a spatial resolution of 10 km (at nadir) (Remer *et al*. 2005). The MOD09 data contain surface reflectance, which was computed from the MODIS Level-1B data for each band (Masuoka *et al*. 1998). This is an estimate of the surface reflectance that would be measured without an atmosphere. The reflectance data in the green, red and NIR bands were used in this study. The MODIS data obtained were reprojected onto the Universal Transverse Mercator (UTM) coordinates using the nearest-neighbour algorithm with the WGS-84 (World Geodetic System). The algorithm does not alter the DN or reflectance value of a pixel, and this does not affect the pixel distribution on a histogram of a NIR, NDVI or NDWI index and the subsequent delineations.

The updated radiance scales were extracted from the head file of the MOD02_QKM data to calculate sensor gain for the green band (G_G) and from the head file of the MOD02_HKM data to calculate G_R and G_{NIR} for each date (NASA 2006). The value of E was 1840 W m^{-2} µm^{-1} for the green band, 1571 W m^{-2} µm^{-1} for the red band and 971.9 W m^{-2} µm^{-1} for the NIR band (Chander *et al*. 2010). The AOT values of 0.47, 0.55 and 0.66 µm and a path radiance of 0.66 µm were extracted from MOD04_L2. The Ångström law was used to calculate AOT at 0.86 µm for the MODIS NIR band (King *et al*. 1999). The values of path radiance at 0.55 and

0.86 µm were estimated using empirical linear relationships between AOT and path radiance for a relatively clear sky (Oliveros *et al.* 1998). Atmospheric transmission, T_s, was calculated using $T_s = e^{-\tau/\cos\theta}$, where $\tau = \tau_r + \tau_a$, τ_a is the aerosol optical thickness and τ_r is Rayleigh optical thickness. τ_r was estimated using the equation $\tau_r = 0.008569\lambda^{-4}\left(1 + 0.0113\lambda^{-2} + 0.00013\lambda^{-4}\right)$, where λ is the wavelength (Hansen and Travis 1974). Mathematically, AOT and SZA are the primary parameters used to determine atmospheric transmission and path radiance for the bands used.

Surface reflectance was extracted from the MOD09 data sets for the green, red and NIR bands. To match the spatial resolution of the red and NIR bands, the 500 m green-band data were re-sampled at 250 m using the nearest neighbour algorithm. Equation (2) was then applied to produce NDVI and NDWI images. The histogram of each index (NIR, NDVI or NDWI) was generated for the delineation of the water surface. The sharp contrast between the water and land surfaces resulted in bimodal histograms. For optimal thresholding, a threshold value was first determined based on the mid-point between the water and land maxima in a generated histogram (Bryant 1999). The threshold value was adjusted slightly such that the extracted features optimally matched both the known lake banks and the enclosed lakes displayed in the false-colour image produced from the green-, red- and NIR-band data for the corresponding date. In some cases where the boundary of an enclosed lake was unclear, the threshold value was adjusted to incorporate image texture techniques in which the variance of the pixel values within a specified neighbourhood around each image pixel was used as a measure of texture (Shoshany and Degani 1992). The optimally determined value was also confirmed with an inspection of the extracted water surfaces using high-resolution Landsat Thematic Mapper (TM) and Advanced Spaceborne Thermal Emission and Reflection Radiometer (ASTER) data. Subsequently, the MODIS-extracted water areas agreed, within a 4% difference on average, with that of water areas extracted from the Landsat TM and ASTER images.

Alternatively, DN values were extracted from the MOD02 data sets for green, red and NIR bands using a similar procedure. The 500 m green-band data were re-sampled to 250 m. The DN data were applied to generate NDVI and NDWI with equation (3). Optimal threshold values were subsequently determined using the same approach as used with the MOD09 data, and the reflectance- and DN-based thresholds were obtained for all the MODIS images.

Alternatively, equations (7a)–(7c) and reflectance-based optimal thresholds were used to obtain the estimated threshold values for the DN-based case. The estimated thresholds were compared with the DN-based values to determine the relationships between the reflectance- and DN-based thresholds. The mean and standard deviation (SD) were calculated for all the variables using a normality test. In addition, a regression analysis was performed to quantify the relationship and to further evaluate the influences of key parameters on the DN-based thresholds.

4. Results and discussion

4.1 *Variation of thresholds for water surface delineation from multi-temporal images*

Figure 1 shows the variation in threshold values used to delineate water surface from multi-temporal images of NIR, NDVI and NDWI. The NIR threshold values for reflectance (NIR_{ref}) range from 0.034 to 0.130. The mean is 0.065 with a one-sigma SD of 0.021 (table 1). The threshold values are generally lower than 0.1, which is attributed to strong absorption by water in the NIR band, distinguishing water from
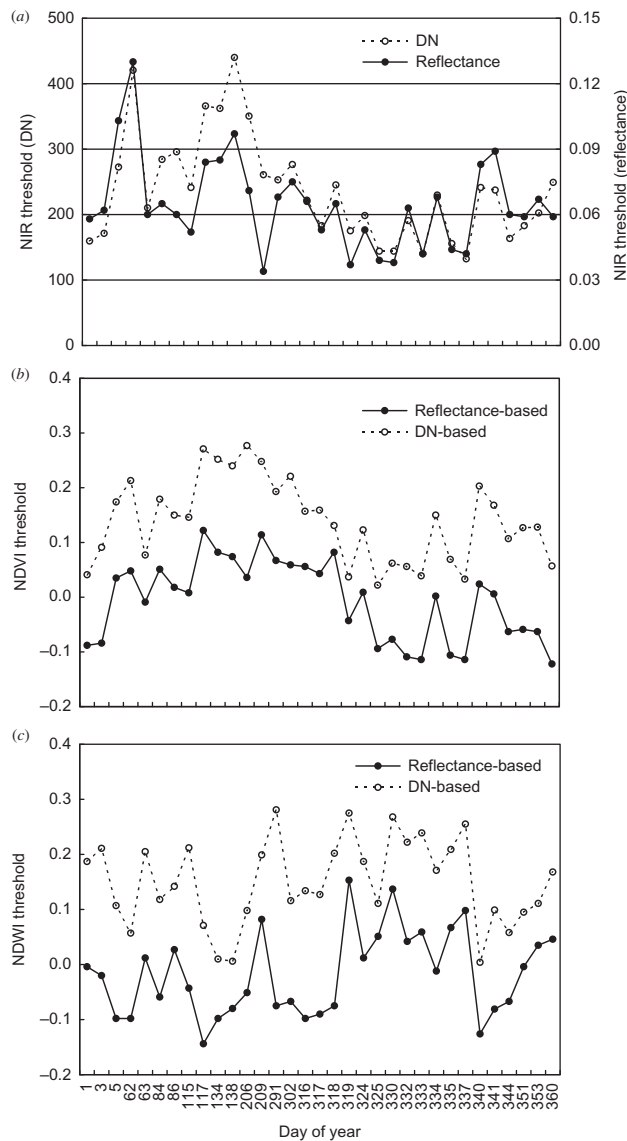
Figure 1. Variation of reflectance- and DN-based thresholds for water surface delineation from multi-temporal MODIS images of NIR (*a*), NDVI (*b*) and NDWI (*c*) in the Poyang Lake region of China in 2008.

soil and vegetation. Alternatively, the NIR thresholds for DN (NIR_{DN}) range from 132 to 440 with a mean and SD of 236 and 80, respectively. As the numerical range of valid DN data is 0–32 767 (NASA 2006), all the NIR_{DN} values are larger than the NIR_{ref} values. Despite this, they display similar fluctuations (figure 1(*a*)).

The reflectance- and DN-based NDVIs have the same numerical range and are comparable in scale. The NDVI thresholds for reflectance ($NDVI_{ref}$) values range from −0.122 to 0.122 with a mean of −0.006 and a one-sigma SD of 0.074 (−0.006 ± 0.074; table 1). The values vary but are generally close to 0. However, the $NDVI_{DN}$

Table 1. Statistics of threshold values for NIR, NDVI and NDWI.

		Min	Max	Mean	SD	RMSE	Difference (%)
NIR	NIR_{ref}	0.034	0.130	0.065	0.021	–	
	NIR_{DN}	132	440	236	80	–	
	$NIR_{DN,est}$	119	437	209	82	–	
	$(NIR)_{DN} - (NIR)_{ref}$	–	–	–	–	–	
	$(NIR)_{DN} - (NIR)_{DN,est}$	− 28	97	27	21	35	11.4
NDVI	$NDVI_{ref}$	−0.122	0.122	−0.006	0.074	–	
	$NDVI_{DN}$	0.022	0.277	0.139	0.075	–	
	$NDVI_{DN,est}$	0.066	0.257	0.159	0.057	–	
	$(NDVI)_{DN} - (NDVI)_{ref}$	0.049	0.241	0.146	0.037	0.152	
	$(NDVI)_{DN} - (NDVI)_{DN,est}$	−0.126	0.083	−0.020	0.043	0.047	13.7
NDWI	$NDWI_{ref}$	−0.144	0.153	−0.017	0.077	–	
	$NDWI_{DN}$	0.004	0.281	0.150	0.078	–	
	$NDWI_{DN,est}$	−0.053	0.273	0.134	0.086	–	
	$(NDWI)_{DN} - (NDWI)_{ref}$	0.060	0.356	0.167	0.062	0.181	
	$(NDWI)_{DN} - (NDWI)_{DN,est}$	−0.151	0.152	0.016	0.060	0.062	9.6

Note: DN, digital number; NIR, near infrared; NDVI, normalized difference vegetation index; NDWI, normalized difference water index; RMSE, root mean square error; SD, standard deviation.

values range from 0.022 to 0.277 with a mean and SD of 0.139 and 0.075, respectively (0.139 ± 0.075; table 1). $NDVI_{DN}$ is generally higher than $NDVI_{ref}$, although they display similar fluctuations (figure 1(*b*)). This similarity leads to the similar SD values determined for $NDVI_{ref}$ and $NDVI_{DN}$ (table 1).

The reflectance-based NDWI ($NDWI_{ref}$) thresholds range from −0.144 to 0.153 (-0.017 ± 0.077; table 1). Similar to NDVI, $NDWI_{ref}$ is generally close to zero with some variability. The DN-based ($NDWI_{DN}$) thresholds are generally higher than the reflectance-based thresholds (figure 1(*c*)), which range from 0.004 to 0.281 (0.150 ± 0.078; table 1). The SD values of $NDWI_{ref}$ and $NDWI_{DN}$ thresholds are close to each other.

The above results reveal that the thresholds vary from day to day. The variation is non-negligible within the same index or between different indices for both reflectance- and DN-based values. Therefore, the differences between the reflectance- and DN-based values or the uncertainties in the DN-based values must be accounted for, with a focus on the reliable use of multi-temporal satellite data.

4.2 *Relationships between reflectance- and DN-based thresholds*

The above analysis demonstrates that the reflectance- and DN-based thresholds had similar temporal fluctuations and differences in magnitude. In this section, we inspect the causative relationship between the reflectance- and DN-based values and discuss what led to the variation in the DN-based threshold values.

With regard to NIR, NIR_{DN} shows a significant relationship with NIR_{ref} (coefficient of determination, $R^2 = 0.58$, $p < 0.005$; figure 2(*a*)), with the NIR_{DN} value being a combined result of surface reflectance and temporal influences in terms of sensor gain (G_{NIR}), SZA, d, path radiance and atmospheric transmission. Combining the parameters with NIR_{ref}, we estimated the DN-based threshold ($NIR_{DN,est}$) using equation (7a). The estimated values agree well with the NIR_{DN} values ($R^2 = 0.92$,
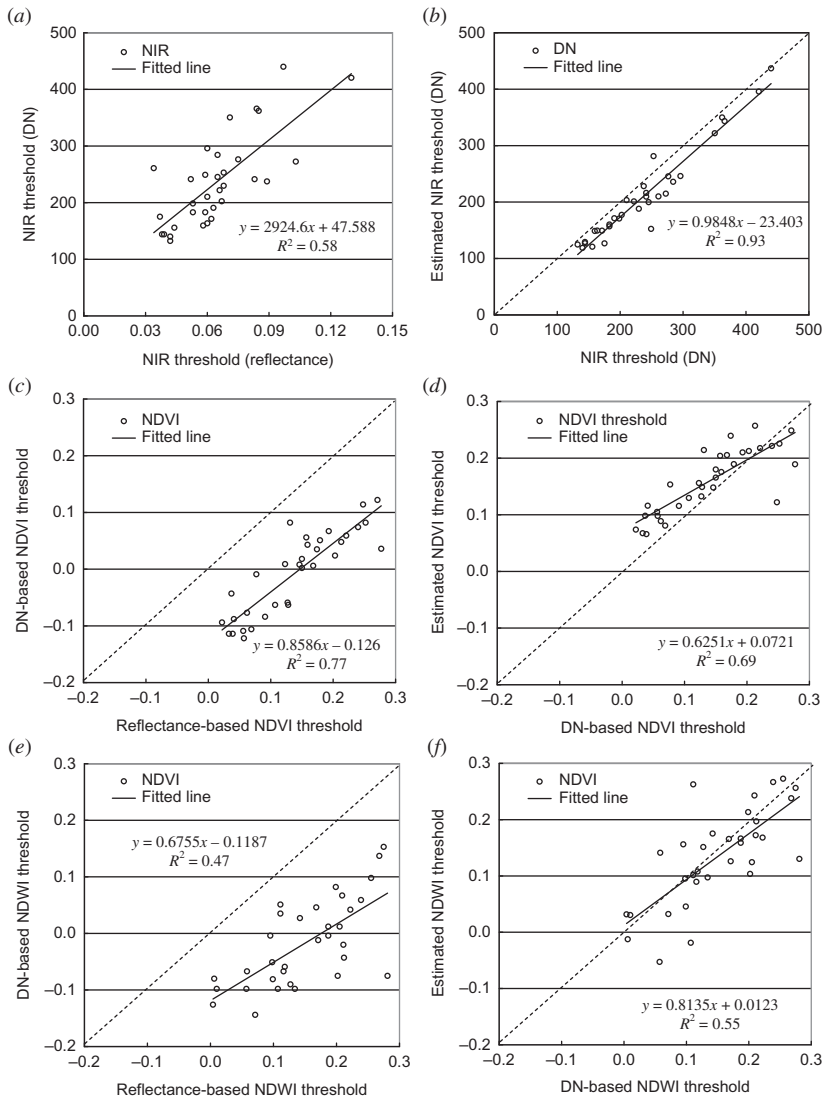
Figure 2.　Relationship between reflectance- and DN-based thresholds for the (*a*) NIR band, (*c*) NDVI and (*e*) NDWI, and that between DN-based and estimated thresholds for the (*b*) NIR band, (*d*) NDVI and (*f*) NDWI.

$p < 0.005$; figure 2(*b*)). The overall NIR_{DN}-to-$NIR_{DN,est}$ difference is 27 ± 21, ~11.4% of the mean of NIR_{DN} thresholds (table 1). The improved R^2 and the small difference also indicate that equation (7a) was effective in accounting for major influences on NIR_{DN}.

$NDVI_{DN}$ is dependent on $NDVI_{ref}$ with $R^2 = 0.77$ ($p < 0.005$) and the mean and SD can be given by 0.146 ± 0.037. Given that the variation in $NDVI_{ref}$ was small (0.074, one-sigma SD), the large difference between $NDVI_{DN}$ and $NDVI_{ref}$ should be accounted for with other sources. With equation (7b), we used the parameters relevant to temporal influences on $NDVI_{ref}$ to estimate the DN-based threshold ($NDVI_{DN,est}$).

As a result, the difference between $NDVI_{DN}$ and $NDVI_{ref}$ decreased from 0.146 ± 0.037 to -0.020 ± 0.043 (the $NDVI_{DN}$-to-$NDVI_{DN,est}$ difference) by 87.3%, and 13.7% difference remained (table 1). The root mean square error (RMSE) between $NDVI_{DN}$ and $NDVI_{ref}$ also decreased from 0.152 to 0.047. The temporal influences were inferred to account for $\sim$90% of the difference between the $NDVI_{DN}$ and $NDVI_{ref}$. Although the correlation coefficient decreased from $R^2 = 0.77$ ($p > 0.005$) to $R^2 = 0.69$ ($p > 0.005$), the thresholds are distributed close to the 1:1 line in the $NDVI_{DN}-NDVI_{DN,est}$ space (figures 2(*c*) and (*d*)). The decrease in R^2 is attributed to the estimation errors in the parameters used in equation (7b).

$NDWI_{DN}$ demonstrates a relatively weak, yet significant, relationship with $NDWI_{ref}$ ($R^2 = 0.47$, $p > 0.005$). The $NDVI_{ref}$ variation is 0.077 (one-sigma SD), less than half of the difference between $NDWI_{DN}$ and $NDWI_{ref}$ (0.167 ± 0.062). Imposing temporal influences on $NDWI_{ref}$ with equation (7c), we obtained the estimate of the DN-based threshold ($NDWI_{DN,est}$). Consequently, the difference between $NDWI_{DN}$ and $NDWI_{ref}$ was reduced to 0.016 ± 0.060 (the $NDWI_{DN}$-to-$NDWI_{ref}$ difference), with 9.6% difference retained (table 1). Correspondingly, the RMSE decreased from 0.181 to 0.062. The temporal influences were inferred to account for over 90% of the difference between $NDWI_{DN}$ and $NDWI_{ref}$. The correlation coefficient increased from $R^2 = 0.47$ ($p > 0.005$) to $R^2 = 0.55$ ($p > 0.005$), and the thresholds are close to the 1:1 line in the $NDWI_{DN}-NDWI_{DN,est}$ (figures 2(*e*)–(*f*)) space.

Overall, the variation in a reflectance-based index is generally lower than its difference from the DN-based counterpart. The temporal influences on a DN-based index can be described quantitatively with equations (7a)–(7c). In the case examined, it accounts for $\sim$90% of the difference between the DN- and reflectance-based thresholds. Quantification of temporal influences reduced the uncertainties relevant to the thresholds. In other words, even with variations, the DN-based index could be used for multi-temporal image delineation with a high accuracy, similarly to the reflectance-based delineation.

4.3 *Influences of key parameters on DN-based thresholds*

Temporal influences on DN-based thresholds can be described by equation (7) and three related key parameters, including band-specific G, SZA and spectral AOT. Table 2 shows the statistics of the parameters used in this study.

G_{NIR} ranges from 12.47 to 12.64 with 12.59 ± 0.05 DNs per unit radiance. Its variation is less than 0.5% with reference to the mean. G_R has a range of 4.75–4.78 with

Table 2. Statistics of sensor gain, SZA and AOT.

	Min	Max	Mean	SD
G_{NIR}	12.47	12.64	12.59	0.05
G_R	4.75	4.78	4.77	0.01
G_G	5.92	6.11	5.99	0.07
G_R/G_{NIR}	0.3773	0.3811	0.3786	0.0011
G_{NIR}/G_G	2.0420	2.1321	2.1033	0.0338
SZA	15.2	56.3	43.4	12.2
AOT (0.55 μm)	0.08	0.77	0.28	0.16

Note: AOT, aerosol optical thickness; NIR, near infrared; SD, standard deviation; SZA, solar zenith angle.

4.77 ± 0.01 DNs per unit radiance, whereas G_G has a range of 5.92–6.11 with 5.99 ± 0.07 DNs per unit radiance. Both G_R and G_G vary by less than 1% of their mean value. In regard to G_R/G_{NIR} and G_{NIR}/G_G, the former had a variation of ∼0.3% and the latter varied by less than 2% with reference to their respective mean values. Overall, the sensor calibration gain has minor effects on the DN-based threshold for the cases examined.

The major influences imposed on the DN-based values came from the Sun–target geometry, as given by the SZA, and from the atmospheric optical properties, as given by the AOT. The NIR_{DN} values have a significant positive dependence on AOT (0.856 μm; figure 3(*a*)). NIR_{DN} rose approximately 103 DNs with an increase of 0.1 AOT. However, NIR_{DN} shows a negative dependence on SZA (figure 3(*b*)). NIR_{DN} changed approximately 50 DNs with a change of SZA by 10°. $NDVI_{DN}$ has a positive, but insignificant, relationship with AOT (figure 3(*c*)). $NDVI_{DN}$ is significantly dependent on SZA with $R^2 = 0.52$, slightly lower than the coefficient for NIR_{DN} versus SZA. $NDWI_{DN}$ does not show a significant dependence on either AOT or SZA, although its variation resulted mainly from temporal factors (figure 2(*f*)).

In general, a DN-based threshold is subject to variation in temporal influences, and in the case examined, the major temporal factors account for over 90% of the variation, but this does not necessarily mean that the variation is definitely dependent on
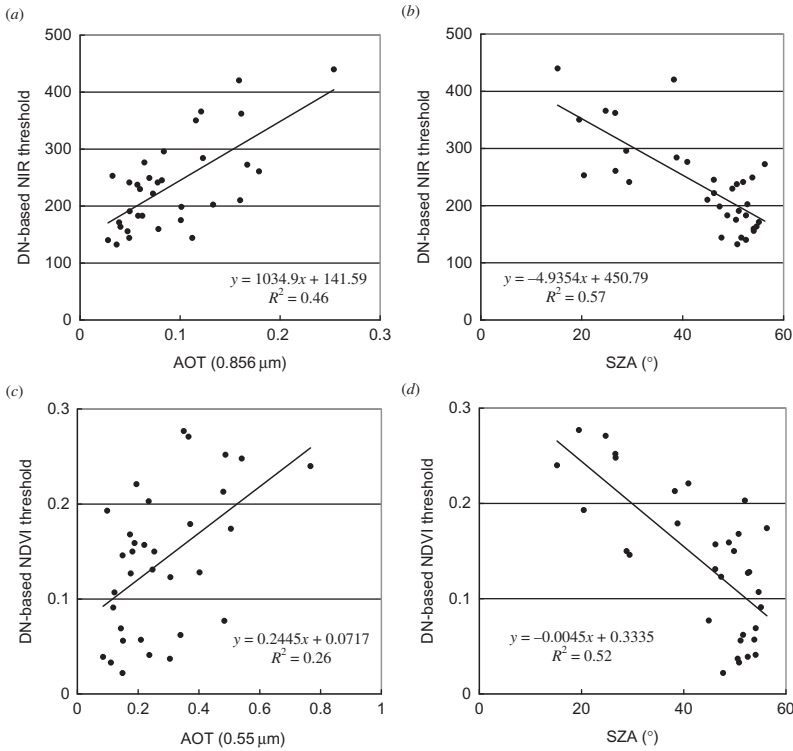

Figure 3.   Relationship of the DN-based threshold with AOT (*a, c*) and SZA (*b, d*) for the NIR band (*a, b*) and for the NDVI (*c, d*).

the key parameters. For multi-temporal remote-sensing applications, our quantification of temporal influences provides an insightful view into the variation in DN-based threshold. These findings improve the knowledge in this field and are valuable for quantitative remote sensing. The methodology developed here is applicable to other indices and for cases in which other objects are extracted.

5.   Conclusions

Based on quantification of temporal influences on satellite images, we conducted a theoretical analysis of variation in a DN-based threshold for water surface delineation from multi-temporal images. We used the single NIR band and NDVI and NDWI indices for delineation with multi-temporal MODIS data. Our results show that a DN-based threshold has a significant dependence on the reflectance-based counterpart, and the former is generally larger than the latter. In the case examined, temporal influences accounted for ~90% of the difference.

Quantification of temporal influences offers a physical explanation of the variation in the threshold and reduces the relevant uncertainties. These findings should be valuable for quantitative remote sensing and for improving the reliability of diverse long-term studies using multi-temporal images. Further studies on the application of the proposed methodology to other indices to extract other objects are necessary.

References

BARNES, W.L., PAGANO, T.S. and SALOMONSON, V.V., 1998, Prelaunch characteristics of the Moderate Resolution Imaging Spectroradiometer (MODIS) on EOS-AM1. *IEEE Transactions on Geoscience and Remote Sensing*, **36**, pp. 1088–1100.

BRYANT, R.G., 1999, Application of AVHRR to monitoring a climatically sensitive playa. Case study: Chott el Djerid, southern Tunisia. *Earth Surface Processes and Landforms*, **24**, pp. 283–302.

CARLSON, T.N. and RIPLEY, D.A., 1997, On the relation between NDVI, fractional vegetation cover, and leaf area index. *Remote Sensing of Environment*, **62**, pp. 241–252.

CHANDER, G., XIONG, X., CHOI, T. and ANGAL, A., 2010, Monitoring on-orbit calibration stability of the Terra MODIS and Landsat 7 ETM+ sensors using pseudo-invariant test sites. *Remote Sensing of Environment*, **114**, pp. 925–939.

CHENG, H.D., JIANG, X.H., SUN, Y. and WANG, J., 2001, Color image segmentation: advances and prospects. *Pattern Recognition*, **34**, pp. 2259–2281.

COMMITTEE ON EARTH OBSERVATION SATELLITES, 2010, Available online at: http://www.ceos. org/ (accessed August 2010).

CRACKNELL, A.P. and HAYES, L., 2007, *Introduction to Remote Sensing*, 2nd ed., pp. 1–304 (London: Taylor & Francis).

GOWARD, S.N., MARKHAM, B., DYE, D.G., DULANEY, W. and YANG, J., 1991, Normalized difference vegetation index measurements from the advanced very high resolution radiometer. *Remote Sensing of Environment*, **35**, pp. 257–277.

HANSEN, J.E. and TRAVIS, L.D., 1974, Light scattering in planetary atmosphere. *Space Science Reviews*, **16**, pp. 527–610.

KING, M.D., KAUFMAN, Y.J., TANRÉ, D. and NAKAJIMA, T., 1999, Remote sensing of tropospheric aerosols from space: past, present, and future. *Bulletin of the American Meteorological Society*, **80**, pp. 2229–2259.

LIU, Y., HIYAMA, T., KIMURA, R. and YAMAGUCHI, Y., 2006, Temporal influences on Landsat-5 Thematic Mapper image in visible band. *International Journal of Remote Sensing*, **27**, pp. 3183–3201.

LIU, Y., NOUMI, Y. and YAMAGUCHI, Y., 2011, Quantifying variability of satellite data in the reflective band for long-term monitoring of the Earth's surface: inference from a multi-temporal relationship between remotely-sensed pixels. *International Journal of Remote Sensing*, **32**, pp. 7717–7730.

MASUOKA, E., FLEIG, A., WOLFE, R.E. and PATT, F., 1998, Key characteristics of MODIS data product. *IEEE Transactions on Geoscience and Remote Sensing*, **36**, pp. 1313–1323.

MCFEETERS, S.K., 1996, The use of the Normalized Difference Water Index (NDWI) in the delineation of open water features. *International Journal of Remote Sensing*, **17**, pp. 1425–1432.

NASA, 2006, MODIS Level 1B Product User's Guide. Available online at: http://mcst.gsfc.nasa.gov/sites/mcst.gsfc/files/file_attachments/M1054.pdf (accessed 29 March 2012).

OLIVEROS, C.S., REYES, F.J.O. and ALADOS-ARBOLEDAS, L., 1998, Determination of aerosol optical thickness from measurements of spectral sky radiance. *Journal of Aerosol Science*, **29**, pp. 1199–1211.

OTSU, N., 1979, A threshold selection method from gray-level histogram. *IEEE Transactions on Systems, Man, and Cybernetics*, **9**, pp. 62–66.

PALA, N.R. and PAL, S.K., 1993, A review on image segmentation techniques. *Pattern Recognition*, **26**, pp. 1277–1294.

REMER, L.A., KAUFMAN, Y.J., TANRÉ, D., MATTO, S., CHU, D.A., MARTINS, J.V., LI, R.-R., ICHOKU, C., LEVY, R.C., KLEIDMAN, R.G., ECK, T.F., VERMOTE, E. and HOLBEN, B.N., 2005, The MODIS aerosol algorithm, products, and validation. *Journal of the Atmospheric Sciences*, **62**, pp. 947–973.

RICHARD, P.S. and MARY, A.T., 1988, Satellite detection of bloom and pigment distributions in estuaries. *Remote Sensing of Environment*, **24**, pp. 385–405.

SCHOTT, J.R., SALVAGGIO, C. and VOLCHOK, W.J., 1988, Radiometric scene normalization using pseudoinvariant features. *Remote Sensing of Environment*, **26**, pp. 11–37.

SHOSHANY, M. and DEGANI, A., 1992, Shoreline detection by digital image processing of aerial photography. *Journal of Coastal Research*, **8**, pp. 29–34.

TANRE, D., DESCHAMPS, P.Y., DEVAUL, C. and HERMAN, M., 1988, Estimation of Saharan aerosol optical thickness from blurring effects in Thematic Mapper data. *Journal of Geophysical Research*, **93**, pp. 15955–15964.

TEILLET, P.M., STAENZ, K. and WILLIAMS, D.J., 1997, Effects of spectral, spatial, and radiometric characteristics on remote sensing vegetation indices of forested regions. *Remote Sensing of Environment*, **61**, pp. 139–149.

VAN LEEUWEN, W.J.D., ORR, B.J., MARSH, S.E. and HERRMANN, S.M., 2006, Multi-sensor NDVI data continuity: uncertainties and implications for vegetation monitoring applications. *Remote Sensing of Environment*, **100**, pp. 67–81.

VERMOTE, E.F., EL SALEOUS, N., JUSTICE, C.O., KAUFMAN, Y.J., PRIVETTE, J.L. and REMER, L., 1997, Atmospheric correction of visible to middle-infrared EOS-MODIS data over land surfaces: background, operational algorithm and validation. *Journal of Geophysical Research*, **102**, pp. 17131–17141.

WOLFE, R.E., NISHIHAMA, M., FLEIG, A.J., KUYPER, J.A., ROY, D.P., STOREY, J.C. and PATT, F.S., 2002, Achieving sub-pixel geolocation accuracy in support of MODIS land science. *Remote Sensing of Environment*, **83**, pp. 31–49.

XIAO, X., BRASWELL, B., ZHANG, Q., BOLES, S., FROLKING, S. and MOORE III, B., 2003, Sensitivity of vegetation indices to atmospheric aerosols: continental-scale observations in Northern Asia. *Remote Sensing of Environment*, **84**, pp. 385–392.

XIONG, X., CHIANG, K., SUN, J., BARNES, W.L., GUENTHER, B. and SALOMONSON, V.V., 2009, NASA EOS Terra and Aqua MODIS on-orbit performance. *Advances in Space Research*, **43**, pp. 413–422.

YUAN, D. and ELVIDGE, C., 1996, Comparison of relative radiometric normalization techniques. *ISPRS Journal of Photogrammetry and Remote Sensing*, **51**, pp. 117–126.

ZHANG, Y., LIU, Y., RUAN, R. and ZHAO, D., 2009, Temporal influences on satellite retrieval of cyanobacteria bloom: an examination in Lake Taihu, China. *Proceedings of SPIE*, **7494, 74942G**, pp. 1–8.

Appendix A. Derivation of equation (5)

The DN for a specific reflective band recorded by a satellite sensor can be related to surface reflectance through the following equations (Vermote *et al*. 1997):

$$DN = GL + B, \tag{A1}$$

$$\rho_{TOA} = \frac{\pi L d^2}{E \cos \theta}, \tag{A2}$$

$$\rho_{TOA} = T_g \left[\rho_a + \frac{\rho T_s T_v}{1 - \rho S} \right], \tag{A3}$$

where G is the band-specific sensor calibration gain (in DNs per unit radiance), L is the at-satellite radiance (W m^{-2} sr^{-1} µm^{-1}), ρ_{TOA} is the top-of-atmosphere (TOA) reflectance and S is the spherical albedo of the atmosphere. Other symbols are described in §2. For $[DN]_0$ taken at the nadir-view when the Sun is at its zenith under an atmosphere-free condition and without sensor degradation, $d = 1$, $\cos \theta = 1$, $T_g = 1$, $T_s = 1$, $T_v = 1$, $\rho_a = 0$ and $S = 0$. From equations (A1)–(A3), we subsequently have

$$[DN]_0 = G \frac{\rho E}{\pi} + B. \tag{A4}$$